

# Tomographic errors from wave front healing: more than just a fast bias

Alison E. Malcolm<sup>1</sup> and Jeannot Trampert<sup>2</sup>

<sup>1</sup>Department of Earth, Atmospheric and Planetary Sciences, Massachusetts Institute of Technology, Cambridge, MA 02139-4307, USA.

E-mail: amalcolm@mit.edu

<sup>2</sup>Department of Earth Sciences, Utrecht University, Utrecht, The Netherlands

Accepted 2011 January 4. Received 2010 December 16; in original form 2010 August 8

## SUMMARY

Wave front healing, in which diffractions interfere with directly travelling waves causing a reduction in recorded traveltime delays, has been postulated to cause a bias towards faster estimated earth models. This paper reviews the theory from the mathematical physics community that explains the properties of diffractions and applies it to a suite of increasingly complicated numerical examples. We focus in particular on the elastic case and on the differences between *P* and *S* healing. We find that rather than introducing a systemic fast bias, wave front healing gives a more complicated bias in the results of traveltime tomography, with fast anomalies even manifesting themselves as slow anomalies in some situations. Of particular interest, we find that a negative correlation between the bulk and shear or compressional velocities may result to a large extent from healing.

**Key words:** Inverse theory; Seismic tomography; Computational seismology; Theoretical seismology; Wave scattering and diffraction; Wave propagation.

## 1 INTRODUCTION

As computing resources grow and the interest in waveform inversion and other full-waveform based inversion methods increases, it is worth revisiting past methods to understand in more detail their limitations so that new results may be correctly compared. When performing ray-based tomography, several assumptions are made, the two strongest being the validity of ray-theory and linearity of the inverse problem. Both of these assumptions break down when the anomalies that perturb the ray paths have large contrasts with the physical properties of the background medium and have sizes of approximately the same order as the wavelength. Part of this breakdown comes from so-called wave front healing, in which waves are diffracted around anomalies and these waves interfere with directly travelling waves resulting in systematic errors in estimated traveltime delay measurements. The name wave front healing should be interpreted carefully as while the measured traveltime delay does decrease further from the anomaly, the waveform still bears the signature of the anomaly even at large distances. Further, the exact character of the decay is dependent on how the traveltimes are picked and on the nature of the source, making straightforward generalizations difficult.

Although there are certainly preceding descriptions, such as those of Claerbout (1976, 1985), the first careful discussion of the effects of diffractions on recorded traveltime delays is given by Wielandt (1987). In this paper, Wielandt uses exact solutions for a plane-wave impinging on a spherical anomaly in 3-D for acoustic wave propagation. He compares picks of the first-arrivals with predicted

ray-theoretical traveltime delays and notes that as the receiver is moved further behind the anomaly, these recorded delays decay due to interference with diffracted waves. He interprets the likely effects of this decay in traveltime as a bias in tomographic models towards a faster Earth. Nolet & Moser (1993) suggest that this may explain discrepancies between normal mode and traveltime tomographic earth models and Montelli *et al.* (2004) use this bias to explain difference between ray-based and finite-frequency kernel-based traveltime inversions. Gudmundsson (1996) continues the discussion of wave front healing, modelling the perturbation of the acoustic wave front as it passes through a lens of heterogeneity. He approximated the recorded delay times by a spatial filter by computing spectral ratios of the ray-theoretical and measured traveltimes. The properties of these filters were then used to estimate the width of the Fresnel zone in various recording geometries. Several other authors have investigated the effects of random media on wave propagation (see e.g. Müller *et al.* 1992; Lomax 1994, and references therein), generally in the context of approximating the wave front after it passes through such anomalies. Nolet & Dahlen (2000), use a parabolic approximation to model the wave front of a wave (as suggested by Snieder 1998) as it passes through a smooth, spherical anomaly and investigate the effects of this anomaly on the approximated wave front by looking directly at the phase delay. They define two regimes, one in which healing simply damps the inverse problem and another in which it poses a real problem. This work is related to that in Hung *et al.* (2001) who attempt to use so-called banana-doughnut kernels to approximately model the effects of wave front healing, an approach that is continued by

Montelli *et al.* (2004). We discuss this work further when we compare our measured arrival times to those predicted with these kernels and those of Spetzler & Snieder (2001). Thore & Juliard (1999) study the impacts of diffractions on the results of reflection tomography studies. Most recently To & Romanowicz (2009) discussed wave front healing in the context of its effect on measured delays in diffracted waves around the core–mantle boundary (CMB); they find these effects to be exacerbated by the presence of thin low-velocity layers above the CMB.

In this paper, we discuss three aspects of this problem that have not been discussed extensively in past work. The first (in Section 2) is the geometrical theory of diffractions, as presented by Keller (1956, 1962, 1985) and discussed from a differential equation formulation specifically for the seismic case in Klem-Musatov *et al.* (2008); from this theory we can predict what configurations are likely to be most strongly influenced by healing, and understand why different picking methods and source wavelets give different results. We illustrate this in detail with 2-D acoustic numerical experiments. We use the acoustic case to setup the problem and investigate questions like the fast/slow asymmetry (also noted in past works Wielandt 1987; Nolet & Dahlen 2000; To & Romanowicz 2009), differences caused by the use of different picking methods and source wavelets, as well as the ability of finite-frequency kernels to compensate for some of the effects of wave front healing. Second, we investigate the phenomena for the elastic case, also in 2-D, and to enable us to discuss the differences in observed healing rates for *P* and *S* waves. Third, to verify that our results are not unique to 2-D, we compute a 3-D example in which we calculate both the traveltimes delays and perform a simple ray-tomography to investigate the impact of healing on the results of a realistic inversion scenario.

For the elastic case, and in particular for the inverse problem section, we focus on imaging anomalies in the deep mantle near the CMB. We focus on this example because of the long wave paths, which maximize the likelihood that measured traveltimes will be incorrect. Such anomalies are similar to those studied by Hung *et al.* (2001). This region is of particular interest for healing studies because, as shown in Masters *et al.* (2000), there is some evidence for anomalies with negative correlations between the *S* and bulk velocity anomalies. Our results indicate that wave front healing does not have the same effect on *P* and *S* waves and thus composite parameters such as the bulk velocity may contain significant errors due to wave front healing alone. We demonstrate, by adding a perturbation near the CMB in PREM that small perturbations in the *P*- and *S*-wave velocities can result in recovered bulk anomalies with incorrect sign.

## 2 PROPERTIES OF DIFFRACTED WAVES

As stated in the introduction, part of the goal of this paper is to highlight past work on diffracted waves done in the mathematical physics community so that some of these rules of thumb from that work may be applied here. Although it has been recognized since wave front healing was first discussed by Wielandt (1987) that the misinterpretation of diffractions as direct waves is at the root of the problem, there does not appear to be a discussion in the seismological literature of exactly how the complicated signatures of wave front healing arise from this relatively simple phenomenon. There are several general references on diffractions in the mathematical physics literature (Babič & Buldyrev 1972; Nussenzveig 1992). The work of Keller, however, found in Keller (1956, 1962, 1985) is perhaps the most intuitive and the most directly applicable

to the present discussion. This work is mentioned in the detailed treatise on diffraction phenomena by Klem-Musatov *et al.* (2008) where various diffraction phenomena are discussed and derived in a differential framework. The theory of Keller is simpler than that given by Klem-Musatov *et al.* (2008), however, and gives us a sufficient geometrical understanding of the effects of diffraction. We thus briefly summarize those results here.

Keller gives three main results, found in a particularly accessible form in Keller (1962). First, the source of diffractions are waves that arrive tangent to the surface around which the wave diffracts. This argument is based on a modified Fermat's principle by which the stationary path containing a curve on the boundary of the anomaly is found. By reciprocity he also concludes that the diffraction recorded must leave the surface along a tangent, thus determining the length of the diffracted path along the diffracting material. This is illustrated for the case of a circular anomaly in Fig. 1. From this argument it is clear geometrically that stations nearer the anomaly will record diffractions that have sensed more of the anomaly having spent more of their traveltimes confined to its surface; this is key to understanding both the amplitude and arrival time of these waves.

Keller's second conclusion is that the amplitude of the diffracted wave decays exponentially during the diffracted portion of its path. He comes to this conclusion by noting that at each point on the diffractor energy is lost to a ray leaving the object and the amplitude of the leaving ray must be proportional to the amplitude of the wave on the surface thus, denoting the amplitude of the diffracted wave by *a* we have

$$\frac{da}{ds} \propto -a, \quad (1)$$

where *s* is the arclength along the object. From eq. (1) it is clear that the amplitude of the diffracted wave must decay exponentially with distance travelled along the diffractor. This attribute of diffracted waves, along with the previously discussed excitation and release points leads us to conclude that stations further from the anomaly will record diffractions which are initially stronger than those recorded nearer the anomaly. Although where diffractions will be strongest will also depend on the geometrical spreading between the anomaly and the station, the fast exponential decay of the starting amplitude is the more important factor, at least over source/anomaly/station separations discussed in this work.

The third and final point of Keller discussed here is that the strength of the diffracted wave is proportional to  $\lambda^{-\frac{1}{2}}$  and therefore in the high frequency limit there are no diffractions, as expected. Keller obtains this result by comparing his asymptotic solution to an exact solution given by Franz (1954). This exact solution is for

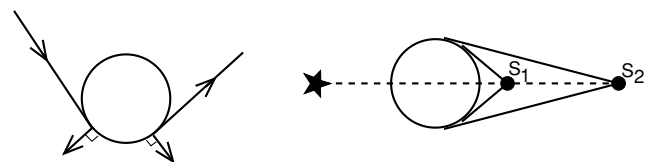


**Figure 1.** According to Keller's theory, diffracted waves are excited and released from the diffracting object along tangents. In the left-hand diagram, this is illustrated for the simple case of a circular anomaly. From the right-hand diagram, we observe that the recorded diffraction will be stronger at station *S*<sub>1</sub> than at *S*<sub>2</sub> because it travels further on the anomaly to arrive at *S*<sub>1</sub> than to arrive at *S*<sub>2</sub> and its amplitude decays exponentially as it travels along the anomaly.

the problem of the scattering of a cylindrical wave by a cylindrical object.

The first two rules of thumb allow us to estimate where diffractions are likely to interfere with first arrivals and thus to understand the observed effects of wave front healing. Although this is a high-frequency theory, it is quite accurate for determining the arrival times and relative amplitudes of diffracted waves even at lower frequencies, similar to ray theory for direct arrivals.

### 3 MODELLING

#### 3.1 2-D acoustic

To the authors' knowledge all of the available literature on wave front healing has dealt only with the acoustic case, so we will begin with that case. Although Chapman & Phinney (1972) discuss elastic diffractions this is in the context of modelling and using core-diffracted phases and not in the context of the impact of diffracted waves on recorded traveltime delays. To & Romanowicz (2009) also discuss the elastic case, but the focus of that paper is not on healing, but again on core-diffracted phases.

These simulations were done using the algorithm discussed in Appendix A1, in which the acoustic wave equation is solved in integral form on the boundary of the anomaly. This method exactly takes into account the radiation condition at infinity and thus has no errors from boundary effects. The method is spectrally accurate and it was verified that the solutions had converged, giving an accuracy of machine-precision. We discuss two similar experiments, depicted in Fig. 2, first with a plane wave incident and second with a point source excitation; for each case we fix the central frequency and change the size and shape of the anomaly. We consider both fast and slow anomalies, where the fast anomaly has a velocity of 1.05 and the slow anomaly has velocity 0.95; the background velocity is 1 in all examples. Unless stated otherwise, for all simulations we use the first-derivative of a Gaussian for the wavelet, with the wavelength given calculated based on the central frequency of this Gaussian.

##### 3.1.1 Plane-wave source

For the plane-wave case, an example data set is shown in Fig. 3. The red lines on these plots show the diffracted traveltimes as predicted

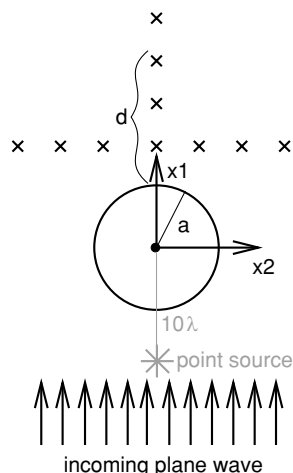


**Figure 2.** Numerical setup for acoustic experiments.

by Keller's geometric theory of diffraction. As was also observed by Wielandt (1987), we are not able to perfectly fit the arrival times of the diffracted waves with Keller's theory. Wielandt interpreted this error as a result of the finite-frequency wave sampling the interior of the anomaly. Although this is consistent with both his and our observations, it is not the case that the wave simply travels along the surface of the anomaly at the interior velocity; this does not significantly change the predicted arrival times. What seems more likely is that some part of the wave travels through the anomaly before contributing to the excitation of the diffraction. To & Romanowicz (2009) observe in their simulations of diffracted waves along the CMB that the diffracted wave is influenced by surrounding structures which may also help to explain this discrepancy.

Having confirmed that Keller's theory does closely explain the diffractions we see in this simple case, we continue to investigate the effects of diffractions on measured traveltimes. The traveltimes as a function of distance behind the anomaly size for several different sized anomalies are shown in Fig. 4. The traveltimes were measured by finding the shift in the peak of the cross-correlation of the measured data with the wavefield from an unperturbed plane wave. For a small anomaly  $a = \lambda$  it is expected that the diffracted waves will arrive at nearly the same time as the direct wave because the two paths are close to the same length. This is exactly what is observed as the initial delay is smaller than predicted by ray theory and then decays rapidly to zero as the difference in arrival time between the diffracted and direct wave decays and the diffraction grows in amplitude. For the larger anomalies the fast/slow asymmetry noted in past studies (Wielandt 1987; Nolet & Dahlen 2000; To & Romanowicz 2009) is clearly visible. The sharp jumps (e.g. at approximately  $100\lambda$  for the fast  $5\lambda$  anomaly) occur when the diffracted wave first becomes stronger than the direct wave. For fast anomalies this results in a change in sign of the anomaly because the diffraction will arrive later than the direct arrival due to its longer path. For the slow case, if the anomaly is large enough, a similar jump is caused by the same mechanism. For the slow case we see an initial enlarging of the traveltime anomaly caused by a broadening of the waveform due to the diffraction. The slight increase in measured delay time for the fast  $5\lambda$  anomaly is due to the shape of the wavelet, which results in a cross-correlation function with multiple peaks; the largest peak is slightly shifted to higher delays because of the distortion of the wavelet due to the interaction of the diffraction and the direct wave. In Fig. 5, we show the waveforms recorded at a distance of  $x_1 = 318\lambda$  for the  $5\lambda$  fast anomaly. In this figure, it is clear that the term wave front healing must be carefully interpreted; there is a clear difference between the two waveforms despite that a traveltime measured by cross-correlation will not see a difference.

In Fig. 6, we illustrate the influence the wavelet and the picking method have on the recovered traveltime delays. First arrivals were picked by finding the first point with absolute amplitude within 10 per cent of the maximum amplitude; all other arrivals were taken as the shift of the maximum of the cross-correlation function as described above. From this we observe that for a fast anomaly, picking first arrivals will result in an accurate estimate of the ray-theoretical delay times. For a slow anomaly, however, picking the first arrivals gives the strongest healing effect. This result is explained by the diffraction arriving before the first arrival of the slow anomaly and after it for the fast anomaly. The effect of the wavelet, when picking time delays with cross-correlations is less pronounced, though clearly the wavelet does play a role in the exact delays that will be recovered. As mentioned above, in all other data shown here, the first-derivative of a Gaussian was used as the wavelet.

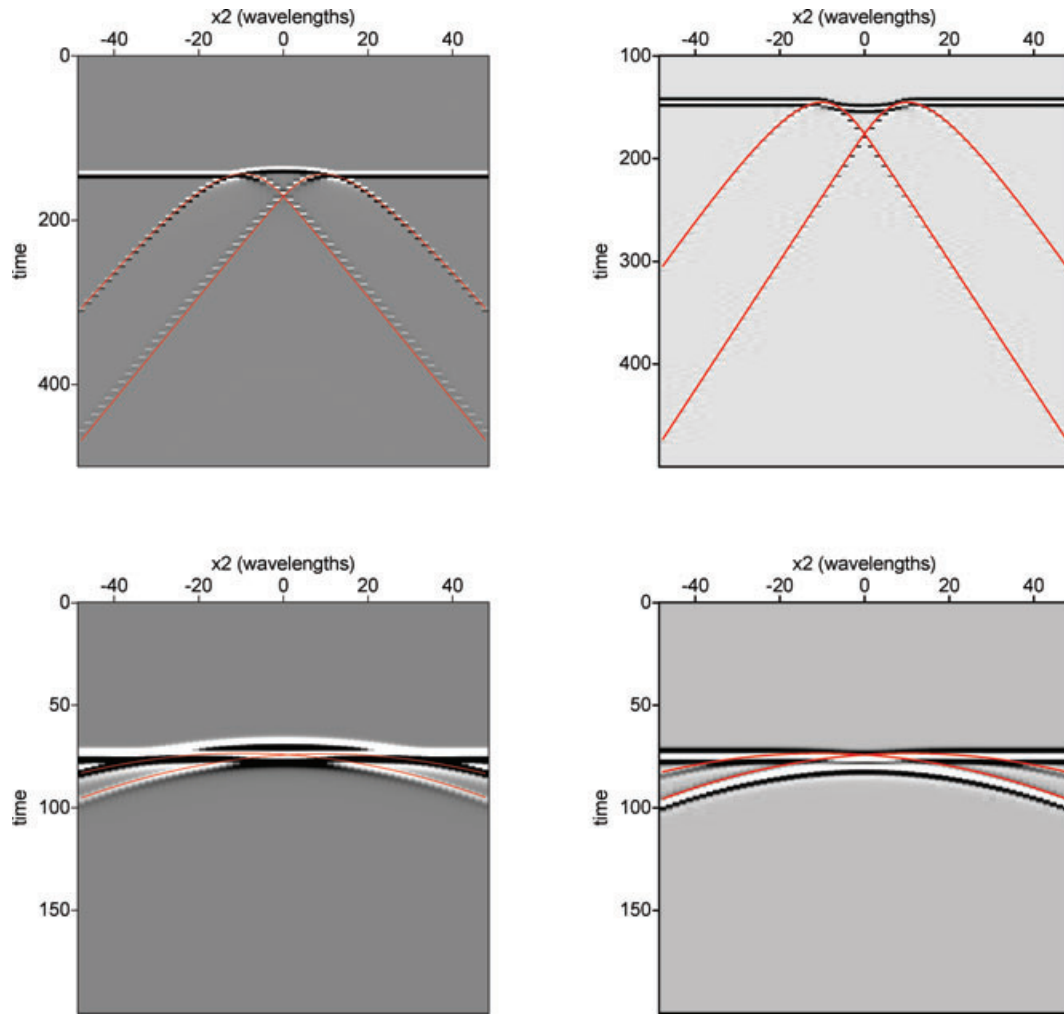


**Figure 3.** Top row: Data along a horizontal line,  $1\lambda$  from the top of an anomaly with a radius of  $10\lambda$  (i.e.  $x_1 = 11\lambda$ ). Bottom row: Data along a horizontal line,  $468\lambda$  from top of the same anomaly. Left is fast anomalies (velocity 1.05 compared with 1.0 outside) and right is slow anomalies (velocity 0.95 within the anomalies). The red lines mark computed diffracted traveltimes with Keller's geometrical diffraction theory. Note that because the figures were generated with a plane-wave source in the frequency domain the origin time is arbitrary; the units are relative to the chosen frequency.

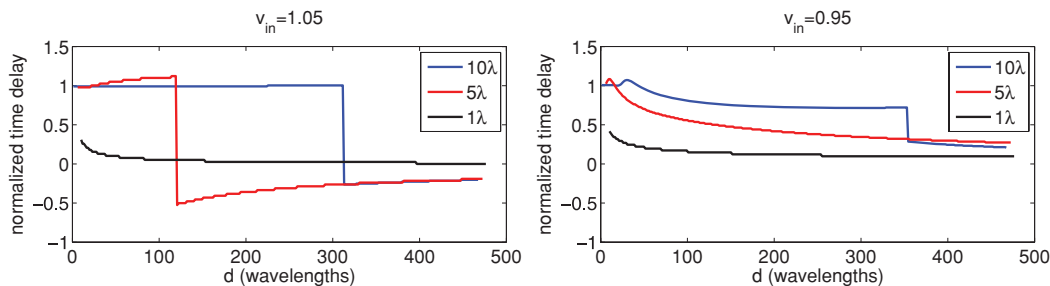


**Figure 4.** Traveltimes delays as a function of distance behind the anomaly for fast (left-hand panel) and slow (right-hand panel) anomalies. Traveltimes are normalized by the expected ray-theoretic delay times.

To conclude this section, we confirm that the results we see are not unique to circular, smooth-sided anomalies. To do this, we use the anomaly depicted in Fig. 7, in which the shape of the anomaly is perturbed with a sinusoidal function. As shown in this figure, the effects of the change in shape are no stronger than the effect of using a different wavelet. Thus, in the remainder of the paper we use only smooth-sided circular anomalies.

### 3.1.2 Point source

Although a plane wave is a good approximation when the source and the anomaly are far apart, it is not a good approximation when the source and anomaly are closer to one another. Of course the root causes of wave front healing remain exactly the same when the plane-wave source is replaced by a point source, the resulting delay

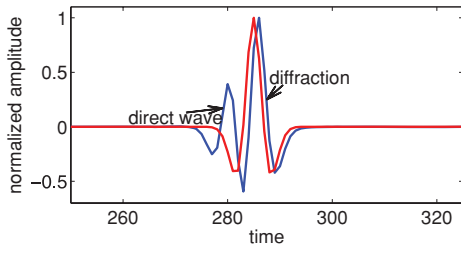


**Figure 5.** Waveform for the  $5\lambda$  fast anomaly, recorded at a distance of  $x_1 = 318\lambda$  along the axis of the anomaly. The red line is the unperturbed plane wave and the blue line is the perturbed wavefield.

time evolution can be quite different and therefore we describe in this section a set of numerical experiments to investigate and explain these differences. The numerical setup is the same as that illustrated in Fig. 2 with the plane wave replaced by a point source at varying position. We move the source only in  $x_2$  as we expect the results to approach that of a plane wave as the source moves further from the anomaly in the  $x_1$  direction. By moving the source, we also break the symmetry of looking at diffractions along the axis of the anomaly. Wielandt (1987) suggested that looking along the axis of the anomaly would create spurious results because the two diffractions (left and right travelling) will arrive simultaneously

only along this axis. By moving the source off-axis we find that this effect does not change the character of the recorded delays, although it does influence the exact decay rate.

Fig. 8 shows comparisons with both different size anomalies and different source locations. For the different anomaly sizes, we observe that healing is much less prevalent in this case than in the plane wave case. The primary cause of this is that the diffractions are excited closer to the source in this case than in the plane wave case. This is because the diffractions are excited when the incoming wave front is perpendicular to the surface of the anomaly; for a plane wave this happens at  $x_1 = 0$  whereas for a point source it happens for  $x_1 < 0$ . Recalling, from the previous section, that the amplitude of the diffracted wave decays exponentially as it travels along the anomaly, and noting that with the closer-to-source excitation location in the point source case the diffraction will travel further along the anomaly, which reduces the amplitude of the diffracted waves. In comparing different source positions, we conclude that the exact behaviour in a given situation is not easily predicted, even though the physics of the underlying phenomena is well understood.

### 3.1.3 Comparison with finite-frequency kernels

It has been suggested (Hung *et al.* 2001) that finite-frequency kernels are able to compensate for the effects of wave front healing.

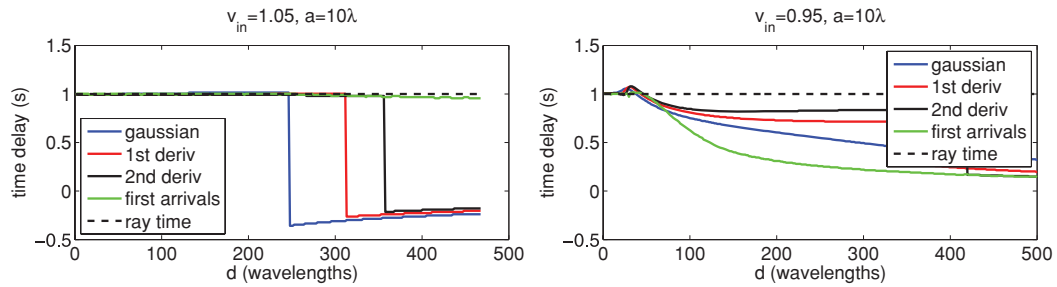


**Figure 6.** Traveltime delays as a function of distance behind the anomaly for fast (left-hand panel) and slow (right-hand panel) anomalies. Different curves represent travel times picked with different wavelets or picking methods, highlighting the effect these things have on observed traveltimes. The label ‘Gaussian’ indicates that a Gaussian is used; this wavelet is then differentiated once to give the ‘1st deriv’ and twice to give the ‘2nd deriv’ curves.

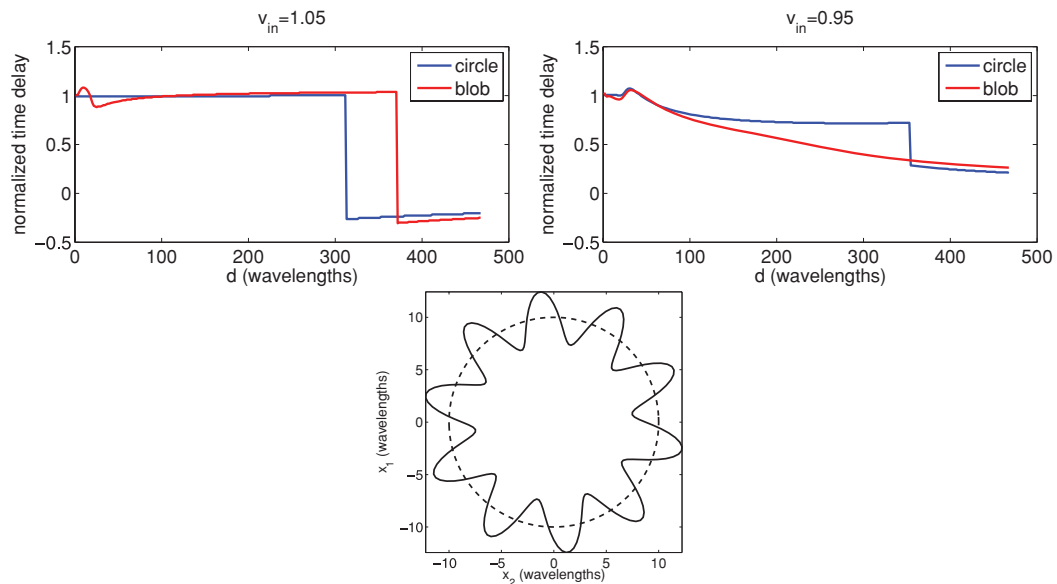


**Figure 7.** Traveltime delays as a function of distance behind the anomaly for fast (top left-hand panel) and slow (top right-hand panel) anomalies, comparing a circular and rugose anomaly. The anomaly itself is shown (with the circular anomaly for comparison) in the lower figure.

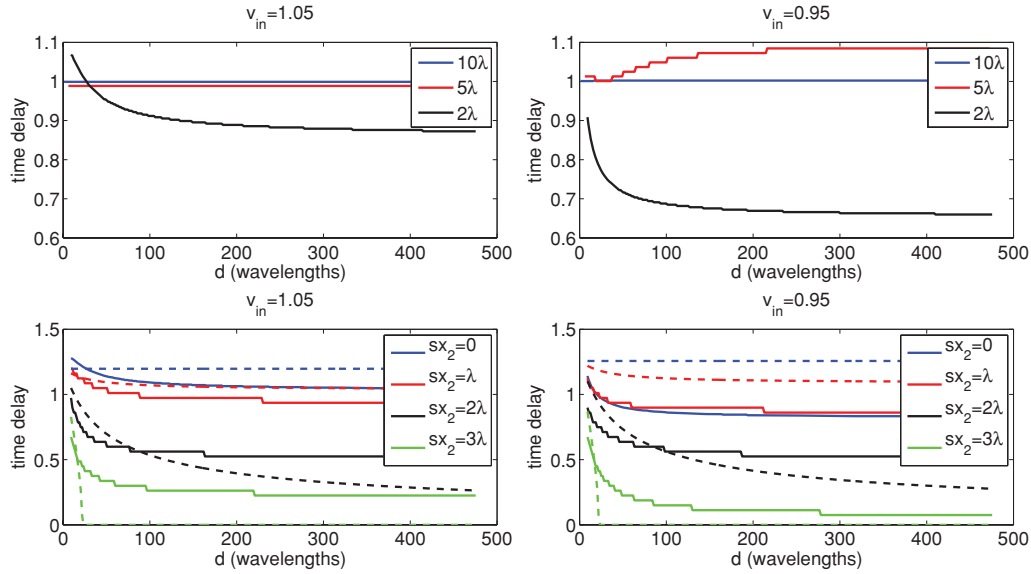


**Figure 8.** Traveltime delays as a function of distance behind the anomaly for fast (left-hand panel) and slow (right-hand panel) anomalies. The top row compares different size anomalies (for the source 10 wavelengths behind the anomaly along its central axis and receivers also along the central axis of the anomaly). The bottom row compares the results for different source positions in the  $x_2$  direction (with the size of the anomaly fixed at  $2\lambda$  and the source  $10\lambda$  from the anomaly in the  $x_1$ -direction). The dashed lines represent the expected ray traveltimes for the correspondingly coloured source position.

To investigate this claim, we now compare the traveltime delays discussed above to predictions from two different finite-frequency kernels. The first kernel we choose to compare to is that of Spetzler & Snieder (2001). This kernel is derived from the Rytov approximation and is valid when the heterogeneities are small compared to the width of the Fresnel zone. Specifically, we compare with their eq. (24) for a point source and their eq. (23) for a plane wave. The second kernel we compare with is the so-called banana-doughnut kernels (Marquering *et al.* 1998, 1999), in particular, we use the 2-D expressions given by Tong *et al.* (1998). This kernel is derived specifically for traveltimes measured with cross-correlations, which is how the delays shown here were measured. In this case, we use eq. (12) from Tong *et al.* (1998) to compute the kernels; a plane

wave source was approximated by moving the source far enough from the anomaly that moving it further did not visibly alter the results. The results, for both a point source and plane wave excitation are shown in Fig. 9.

The results of this comparison are perhaps not surprising. We find that the kernels approximate the traveltime delays fairly well for small anomalies, excited by a point source, and less well for larger anomalies excited by a plane wave. For the kernels derived in Spetzler & Snieder (2001), the larger anomalies are clearly outside the range of the theory and so it is not particularly surprising that the theory breaks down, even though the ray-theory approximation becomes better for larger anomalies. For the kernels in Tong *et al.* (1998), we would expect to see better agreement with the larger

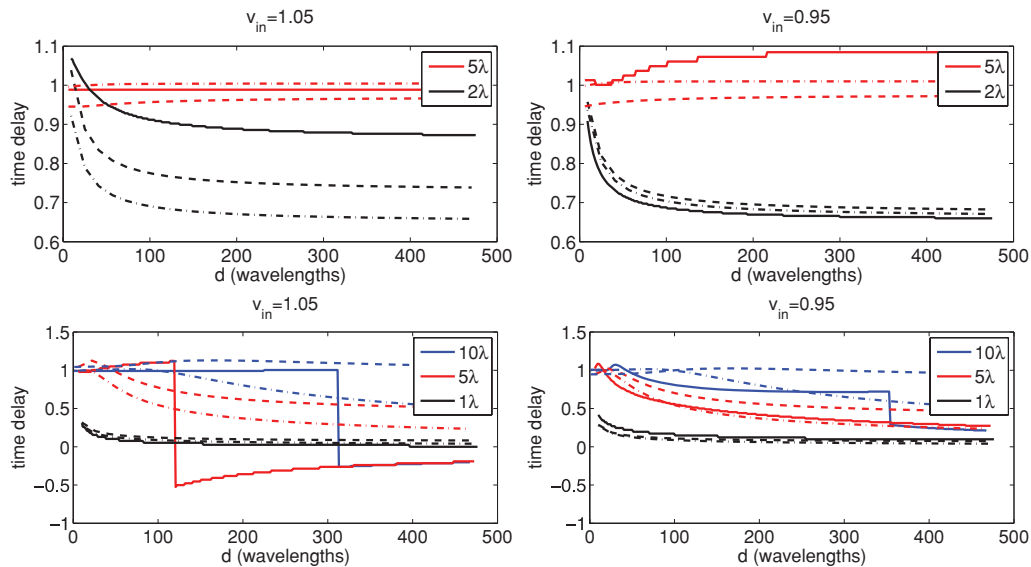


**Figure 9.** Comparison between recorded traveltime delays and estimated delays using two different sensitivity kernels. The kernels of Tong *et al.* are shown in dot-dashed lines, while those of Spetzler & Snieder are shown in dashed lines. The colour corresponds to the size of the anomaly, as defined in the legend. The top plots are for a point source, located  $10\lambda$  behind the anomaly. The bottom plots are for a plane wave source.

anomalies, which is the case for a fast perturbation. None of the kernels is able to account for the jump in estimated traveltime delay caused by the cross-correlation function picking the diffraction instead of the direct wave (as noted by Nolet & Dahlen 2000; Hung *et al.* 2001). This is because they are all based on a single-scattered approximation (Rytov or Born) that does not take the diffractions into account explicitly. These results indicate caution in using finite-frequency theories in place of full-wave theories; the approximation may not be any better than ray theory. There are several reasons that we reach a different conclusion from Tong *et al.* (1998). First, we look much further behind the anomalies than they do, making the effects of healing more important. Second, they use smooth anomalies, while we use sharp ones. Which is more appropriate depends of course on the precise structure of the subsurface. Finally, in several of the examples discussed by Tong *et al.* (1998) they use a weighted cross-correlation to emphasize the earliest part of the arriving pulse. This essentially results in the picking of first-arrivals, which as we discussed previously removes some of the healing effects, at least for fast anomalies.

### 3.2 2-D elastic

The results shown in the previous section for the acoustic case setup the problem and give us a starting point for understanding the effects of wave front healing we can expect as we move to more realistic situations. Although acoustics allows us to understand several key factors affecting wave front healing, to understand its effects in the real Earth requires at least an elastic model. As a first step in that direction, in this section, we address the case of healing for elastic waves in two-dimensions. We again use a boundary integral method, similar to that used in the acoustic case; the elastic extensions are described in A2. The experimental setup is the same as that depicted in Fig. 2, with the exception that we now have two directions in

which we can excite a point source and two types of plane wave excitations to consider. We again consider two cases, the first with plane wave excitations and circular anomalies. In the second case, we use a point source excitation and an elliptical anomaly to mimic the types of anomalies one might encounter in the lower-most mantle when doing tomographic studies; this last example is similar to the anomaly investigated in the 3-D elastic case.

#### 3.2.1 Plane wave excitation

In Fig. 10, we show the delay times resulting from the interaction of an incoming plane wave with a circular anomaly. In this case, the anomaly is in the Lamé coefficients,  $\lambda$  and  $\mu$ . We use  $\lambda = \mu = \rho = 1$  for the background giving  $V_p = 1$  and  $V_s = 1/\sqrt{3} \approx 0.58$ ; both  $\lambda$  and  $\mu$  are increased to 1.1 for the fast case and reduced to 0.9 for the slow case; the resulting  $P$  and  $S$  velocities are given in the titles of the plots in Fig. 10. In comparing this figure with the acoustic results in Fig. 6, we observe that the healing for the  $P$  wave is fairly similar to the acoustic case, with the exception of the  $5\lambda$  anomaly that does not display the same jump as was seen in the acoustic case. This implies that most of the healing is taking place due to interactions of the diffracted  $P$  wave with the direct  $P$  wave. This is not surprising since the incident wave is a  $P$  wave and because of the higher velocity of a  $P$  wave any converted phases will arrive later than the not-converted phases. For the  $S$  wave there is no significant difference between the elastic results and the acoustic ones. This indicates that the  $P$ -diffracted waves are not strong enough, in this case, to interfere with the direct  $S$  wave. In comparing the healing of the  $P$  and  $S$  cases, we observe, however, that the traveltimes do not always evolve in the same way, for example the behaviour of the  $5\lambda$  fast anomaly and the  $10\lambda$  slow anomaly are quite different between the  $P$  and  $S$  delays. This indicates that care must be taken in interpreting results that rely on both  $P$ - and  $S$ -wave data such as the bulk wave speeds.

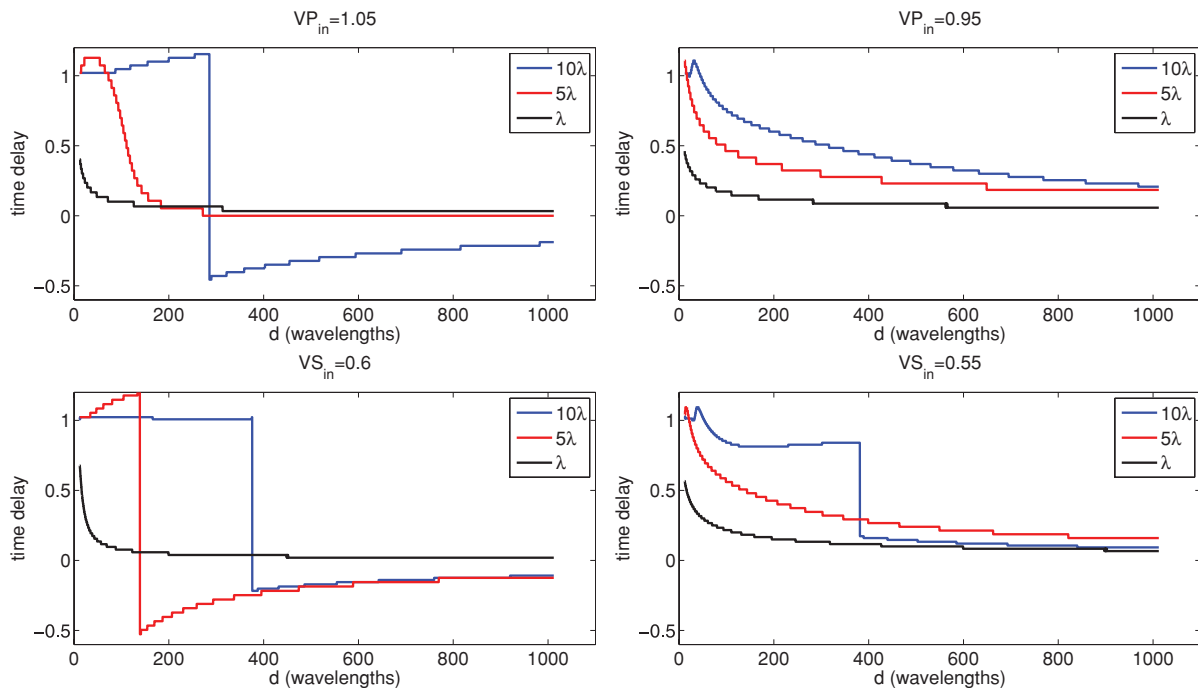


**Figure 10.** Delay times for elastic wave propagation with a circular anomaly, with varying radii. Top panel: For an incoming  $P$ -polarized plane wave. Bottom panel: For an incoming  $S$ -polarized plane wave. We look at delay times only for the same wave type as the incident wave because there is no direct wave of the other phase. On the left-hand side are fast anomalies and on the right-hand side slow.



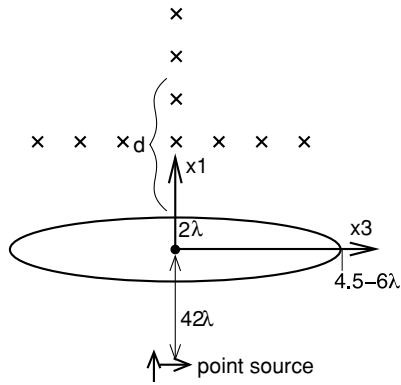


**Figure 11.** Setup for the 2-D elastic experiments to mimic an anomaly in the deep mantle.

### 3.2.2 Point source excitation, elliptical anomaly

For a point source excitation, we found that the results for a circular anomaly were not that different than what would be expected from the plane wave results along with the point source results in the acoustic case. We instead use a 2-D simplification of a setup to measure traveltimes delays for a deep-mantle anomaly located near the CMB with 400 km thickness and  $30^\circ \times 50^\circ$  lateral extent, as measured by an  $ScS$  (or nearly equivalently an  $S$ ) wave with  $\Delta = 61.5^\circ$ . To scale this problem, we assume a  $P$ -wave velocity of  $10 \text{ km s}^{-1}$  and a 20 s period wave, giving a wavelength of 200 km to which everything is scaled. Fig. 11 shows the setup, giving the relevant distances in wavelengths. We continue to look at signals transmitted through the anomaly in this case, and simply ensure that the wave travels the appropriate number of wavelengths between the source and the anomaly and the anomaly and the receiver (in this case 42 wavelengths on either side of the anomaly). We

investigate two anomalies, one with the smaller  $30^\circ \approx 4.5\lambda$  and the other with the larger  $50^\circ \approx 6\lambda$  lateral extent. We also use two point source excitations, one oriented along the  $x_1$ -direction and the other oriented along the  $x_3$ -direction. We use for the background model  $\lambda = \mu = 100$ ,  $\rho = 3$  and look at two perturbations, both of which satisfy  $\frac{\delta V_s}{V_s} = 2 \frac{\delta V_p}{V_p}$  the small ( $\delta V_s/V_s = 2$  per cent) contrast has parameters  $\lambda = 102$  and  $\mu = 96$  and the large contrast ( $\delta V_s/V_s = 20$  per cent) has parameters  $\lambda = 115$  and  $\mu = 64$ ; the density is fixed in all experiments. In these experiments we found that there was little enough difference between the cases shown here and the case when the anomalies have opposite sign that we do not include those results here.

Fig. 12 shows the recorded traveltimes delays for these models, with the dashed lines the 2 per cent anomaly and the solid lines the 20 per cent anomaly. The delays for the specific case of an anomaly at the base of the mantle, one should look at  $d = 42$ ; here we plot a range of distances to show the decay of recorded traveltimes with distance from the anomaly. Note that in this case the source is directly behind the anomaly. We expect that moving the source laterally would have a similar results as in the previous subsection. It does not appear that the difference in anomaly strength has a significant effect on the resulting decay of traveltimes over this range of distances. With a point source, the difference in healing of the  $P$  and  $S$  waves is apparent. This emphasizes the need to carefully interpret composite properties as the errors caused by wave front healing are not likely to be the same for both wave types.

### 3.3 3-D elastic

In this section, we assess whether or not our conclusions from the 2-D examples discussed above are likely to hold in the 3-D case. To this end, we use the SPEC-FEM (Komatitsch & Tromp 2002a,b) code to simulate 3-D wave propagation in the whole Earth. We

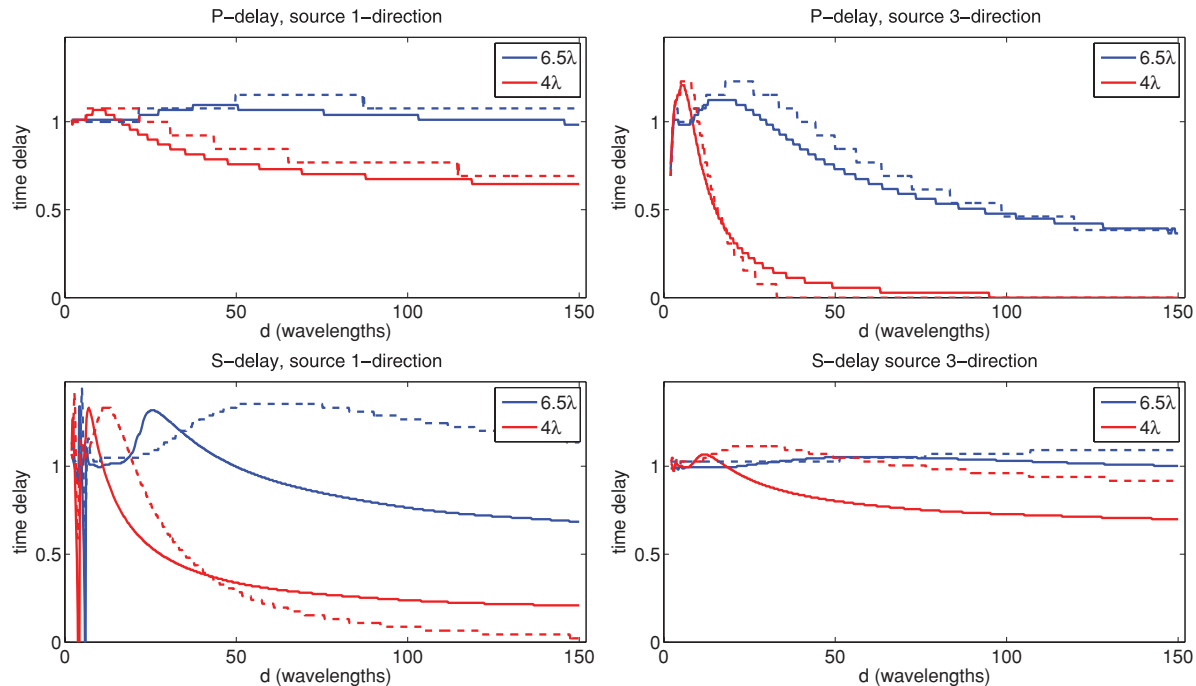


**Figure 12.** Delay times for elastic wave propagation with an elliptical anomaly, with varying radii, with a 2 per cent velocity contrast. Left: For an point source with displacement in the 1-direction. Right: For a point source with displacement in the 2-direction. Top panel:  $P$ -wave delay times. Bottom panel:  $S$ -wave delay times. Solid lines are the 20 per cent contrast and the dashed lines are for a 2 per cent contrast.



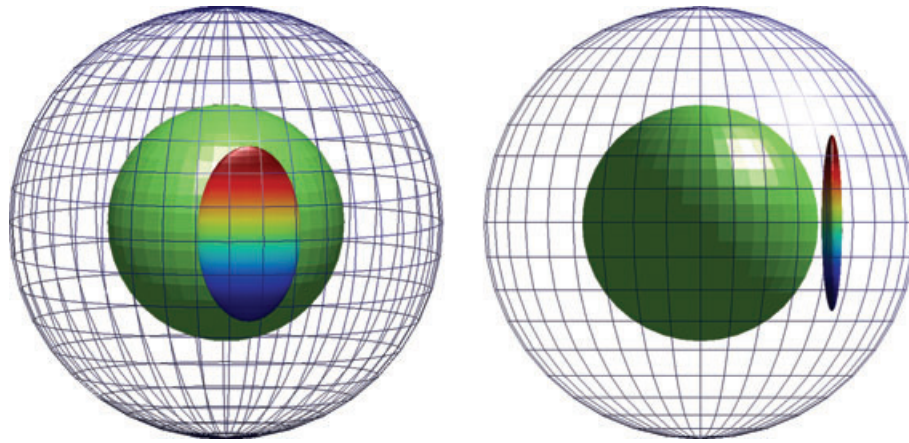


**Figure 13.** The anomaly for the 3-D case is the coloured ellipsoid, just outside the core (shown in green); the mesh is the surface of the Earth.

explore perturbations from PREM (Dziewonski & Anderson 1981), and focus in particular on anomalies near the CMB. We choose this location because it is in these regions that the waves have travelled furthest and thus are most likely, based on the results of the previous sections as well as those of past works, to have experienced significant healing. From our 2-D studies, we expect that the largest impact of wave front healing will not be on the recovered  $P$ - and  $S$ -velocity anomalies but will instead be on composite properties such as the bulk-velocity. To study this, we are particularly interested in the anomalies found by Hutko *et al.* (2008), Masters *et al.* (2000) and we thus base our anomaly on these findings. The anomaly is depicted in Fig. 13; it is an ellipsoid, with radius 300 km in the depth direction, with radii of 2590 and 1550 km in the north/south and east/west directions, respectively. This is consistent both with the anomaly observed by Masters *et al.* (2000) and that studied in the previous subsection. The anomaly is centred beneath the equator and prime meridian with centre 400 km above the CMB and has perturbations of 4 and 2 per cent for  $S$ - and  $P$ -wave velocities, respectively.

We used SPECFEM (Komatitsch & Tromp 2002a,b) to simulate the response to four earthquakes, with locations given in Table 1. The reference seismograms are calculated in anisotropic PREM, including 1-D attenuation, gravity and ellipticity. The 3-D model consists of elastic perturbations due to the ellipsoid added to PREM. For all four quakes, we used the CMT solution of the 1994 Bolivian earthquake, located at a depth of 647 km. Although the radiation pattern of the source is important for the healing observed at a particular station, we do not expect it to be a key factor here because we are recording the response on a network centred on the earthquake location. The response was recorded at an equally sampled global network of stations, placed on concentric circles centred on the source location with  $2.5^\circ$  increment in radius and  $18^\circ$  angular increments for a total of 836 stations for each source position with  $\Delta$  between  $5^\circ$  and  $120^\circ$ ; the array is shown in Fig. 14 for the

fourth earthquake location (for each earthquake this array is moved to be centred on the quake location). Both  $P$  and  $S$  delay times were measured on data rotated into vertical, horizontal and transverse components, by cross-correlating seismograms modelled in an unperturbed PREM to those with the added 3-D elastic perturbation. For the  $P$  arrival a window was chosen based on the expected ray-arrival and the recorded vertical component waveform was then cross-correlated with the unperturbed waveform in the pre-defined time window. A similar procedure was followed for the  $S$  arrivals on the transverse component. At the discretization used, we expect the simulations to be accurate down to 30 s period; we filtered the simulated waveforms with a second order Butterworth filter with corner frequencies at 50 and 100 s periods, resulting in a ratio of structure over wavelength between 1.5 and 5.

The results are shown in Figs 14 and 15, where both the recorded delay times and the anticipated ray arrival times are shown. For both the fast and slow cases, we observe that the recorded arrival times are a smaller in amplitude, smeared, version of the expected ray delays. The ray delay times are more compact in space because only certain stations will have a ray that passes through the anomaly; a finite-frequency wave will pass through the anomaly over a much larger range in station position. There is little difference between the fast and slow anomalies, although for the slow case we do notice localized significant fast delay times near the poles. This indicates that diffractions are interfering with the recorded delay times.

#### 4 INVERSION

Using the data set computed in the previous section, we now investigate the inverse problem to determine the impact of the trends observed in the traveltime data, in particular the concerns about the bulk anomaly. To this end, we performed a traveltime inversion following the method of Ritsema *et al.* (2004). From the 3344 earthquake/station pairs, we measured 1125 and 488 non-zero delay times for  $S$  and  $P$  arrivals, respectively. The difference in the number of non-zero picks is likely due to differences in sampling for different wave types, the smaller  $P$  anomaly strength and the effect of healing depending on wave type. Fig. 16 shows the number of rays sampling  $10^\circ \times 10^\circ \times 100$  km bins in latitude, longitude and depth, respectively. Given this ray coverage, and its similarity for  $P$  and  $S$  waves, we expect the model to be relatively well constrained by this data set despite the relatively small number of earthquakes.

**Table 1.** Locations of the earthquakes used to attempt to recover the CMB anomaly.

Quake number	Latitude ( $^\circ$ )	Longitude ( $^\circ$ )
1	30	0
2	0	30
3	-30	0
4	0	-30

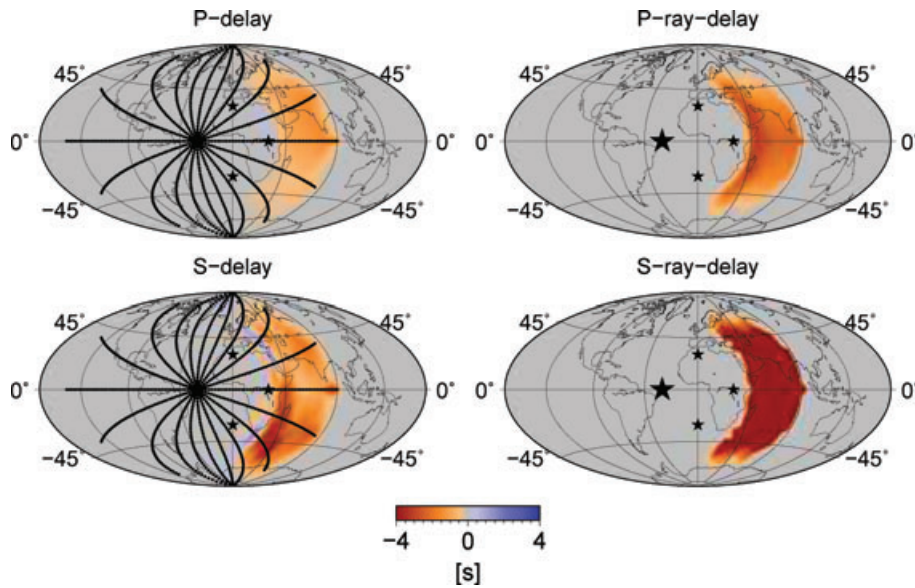


**Figure 14.** Measured (left-hand panel) and ray (right-hand panel) traveltimes for the 3-D model with a fast anomaly near the CMB. Top panel:  $P$ -wave delays. Bottom panel:  $S$ -wave delays. The four earthquake locations used in this study are shown with stars. The traveltimes delays are shown for the earthquake marked with the larger star. The circular symbols on the measured delay plots show the station locations for the earthquake for which delays are shown. This same array is rotated to be centred on each earthquake for its recording. We chose to measure delays out only to  $\Delta = 120^\circ$  as this is the maximum epicentral distance at which we expect to see a direct  $P$  wave; we measure  $S$ -delays out to the same distance to avoid biasing the results for the bulk anomaly.

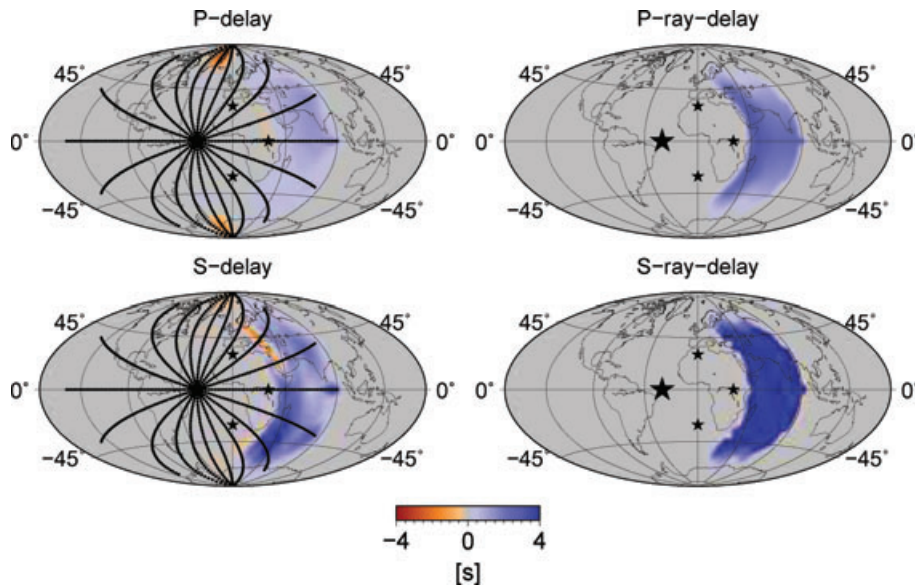


**Figure 15.** Measured (left-hand panel) and ray (right-hand panel) traveltimes for the 3-D model with a slow anomaly near the CMB. Top panel:  $P$ -wave delays. Bottom panel:  $S$ -wave delays. The four earthquake locations used in this study are shown with stars. The traveltimes delays are shown for the earthquake marked with the larger star. Station locations are shown on the measured delay plots. We chose to measure delays out only to  $\Delta = 120^\circ$  as this is the maximum epicentral distance at which we expect to see a direct  $P$  wave; we measure  $S$ -delays out to the same distance to avoid biasing the results for the bulk anomaly.

We now attempt to recover a model using 21 vertical splines and spherical harmonics up to degree 8, resulting in 1701 unknowns. We chose this parametrization so that the number of unknowns would be smaller than the number of data (3344) reducing the effects of regularization, while still being fine enough to be able to recover the input anomaly. In Fig. 17, we show a plot of unexplained variance as a function of independently inverted parameters [quantified by the trace of the resolution matrix,  $\text{trace}(R)$ ], from which we choose

a value of  $\text{trace}(R)$  of 185 as there is little reduction in data misfit after this point.

The results of this inversion are shown in Figs 18 and 19. We observe the following:

- (i) The anomaly shape is slightly better recovered for  $P$  velocity than for  $S$ ; this is likely due to slight differences in sampling for the different phases.

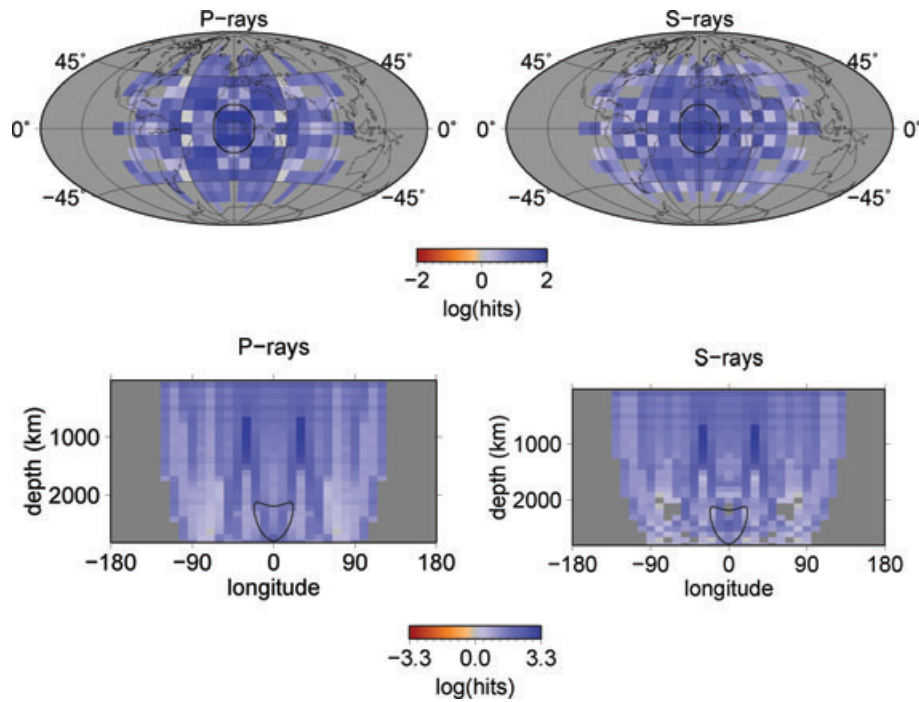


**Figure 16.** Top panel: Ray counts at a depth of 2500 km. Bottom panel: Ray counts at latitude  $0^\circ$ . From these plots we conclude that we have sufficient ray coverage for the inversion despite the relatively small number of earthquakes. The bin size is  $10^\circ$  in both latitude and longitude, and 100 km in depth.

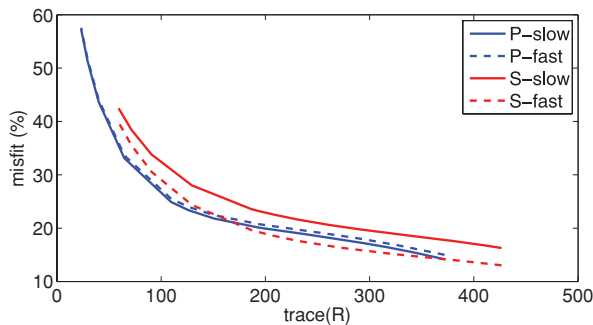


**Figure 17.** Data misfit as a function of resolution. From this figure we choose our regularization so that  $\text{trace}(R) = 185$  as the data fit does not improve significantly beyond this point.

(ii) Both of the anomalies are underestimated in amplitude, which is not surprising as the traveltime delays were consistently underestimated (Figs 14 and 15).

(iii) For both fast and slow anomalies, the recovered bulk anomaly has the incorrect sign.

These results indicate that the interpretation that wave front healing biases results to smaller faster anomalies is probably too simplistic for a fully elastic Earth. The effects are significantly more complicated and are different for  $P$  and  $S$  waves, as well as dependent on the distance from the source to the anomaly and the anomaly to the station complicating the interpretation of ray-based tomography results. Given the results shown in Fig. 6, it is reasonable to expect that different picking algorithms may change the details of the results. From this figure we would expect those changes to be minor as the waves travel approximately 50–100 wavelengths from the anomaly to the receiver; in this region the difference between

different picking methods are relatively small. Even were the expected differences larger, we do not expect this to change our final conclusion with respect to the bulk anomaly, as this comes from differences in healing for  $P$  and  $S$  waves. It seems plausible that these differences will remain provided the same picking strategy is used for both phases.

To ensure that the difference in sign of the bulk anomaly is not a result simply of our choice of regularization, we plot in Fig. 20 the correlation of the recovered  $P$  and  $S$  velocity anomalies at the centre of the anomaly as a function of the regularization [again quantified through  $\text{trace}(R)$ ]. From this we see that the observation that the bulk anomaly is of incorrect sign is independent of the choice of regularization.

## 5 DISCUSSION

Thus far, we have reviewed a simple theory to explain the strength and timing of diffractions and have shown numerical examples that illustrate wave front healing in a variety of situations. Here, we attempt to synthesize and combine these results to better highlight situations in which wave front healing is likely to seriously impact the results of ray-based traveltime tomography inversions.

From the acoustic case, we determined that fast anomalies will appear slow for a plane-wave source (or equivalently a point source far from the anomaly) and a distant receiver. This results from the larger amplitude of the diffracted waves far from the anomaly and indicates that not all bias from wave front healing will act to make the Earth appear faster than it is. From Fig. 6, we also note that this effect can be essentially entirely removed for a fast anomaly by replacing the cross-correlation picking by the picking of the first arrival. This indicates that picking using methods such as that suggested by Bolton & Masters (2001) may reduce the impacts of wave front healing for fast anomalies. This is not the case for slow



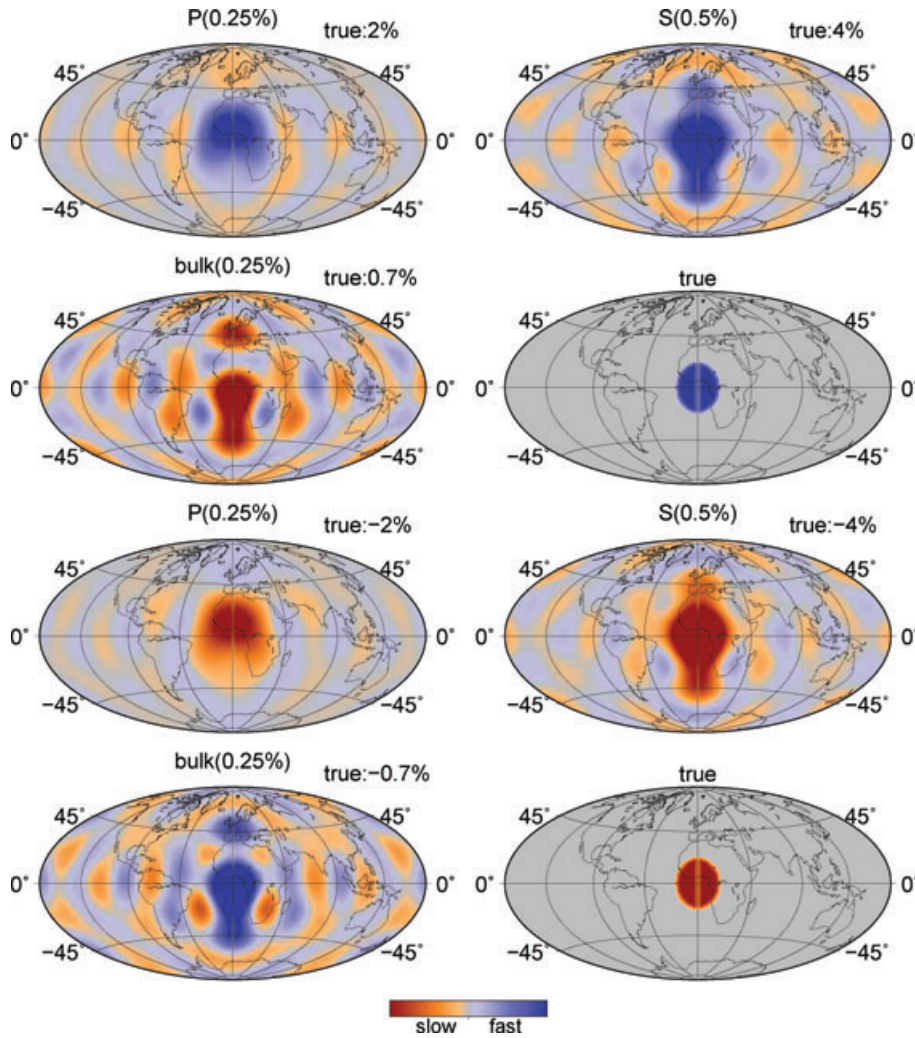


**Figure 18.** Inversion results, at 400 km above the CMB, through the centre of the anomaly. The number in brackets gives the maximum values of the colour scale for the anomaly; the true number is also given in the title. The ‘true’ plots show the correct anomaly. Note in particular that the bulk anomaly has the incorrect sign for both fast and slow perturbations.

anomalies, however, where we found healing to be strongest when picking first arrivals. This leads us to conclude, as Wielandt (1987) did, that when such techniques (or simply first-arrivals) are picked the bias is indeed toward faster earth models, if the Earth were purely acoustic. The exact nature of the bias introduced by using finite-frequency theories, such as those of Tong *et al.* (1998), or Spetzler & Snieder (2001), is less clear as these theories do better in some situations than in others. For example, both are quite accurate for an anomaly of  $1\lambda$ , but neither is accurate for an anomaly of  $5\lambda$ , particularly when that anomaly is far from the source. This leads us to conclude that picking first arrivals, using ray theory, and expecting a result that is biased towards fast anomalies is the most consistent approach that we are aware of short of full-waveform methods, for acoustic models.

For the elastic case, as expected there are further complications. We do not find that the interference of *S* diffractions with directly travelling *P* waves or vice versa was a particular problem for the examples studied here, but we do find that the excited diffraction strength is often different for the two wave types resulting in different rates of healing for the same anomaly and source. Although the exact evolution of the delay times with distance is different for dif-

ferent source excitations and anomaly sizes, this result is robust over both these parameters. This, along with the results of our inversion study, lead us to the conclusion that the interpretation of composite parameters such as the bulk modulus or bulk velocity contrast is strongly influenced by healing in a way that may be difficult to predict *a priori*. In the real Earth, attenuation plays a significant role. While PREM contains a 1-D attenuation model, we neglected 3-D attenuation effects which are thought to be small compared to 3-D elastic effects (e.g. Tibuleac *et al.* 2003). Furthermore, the picking method that may also influence the results. However, it seems reasonable to conclude that particular care must be taken when there is a difference in sign between the bulk and shear or compressional velocities as we have shown that this can result simply from healing and not from a physical difference.

## 6 CONCLUSIONS

From the results shown here, we conclude that wave front healing is a pervasive phenomenon that can largely, if not entirely, be explained by the theories of geometrical diffraction developed in

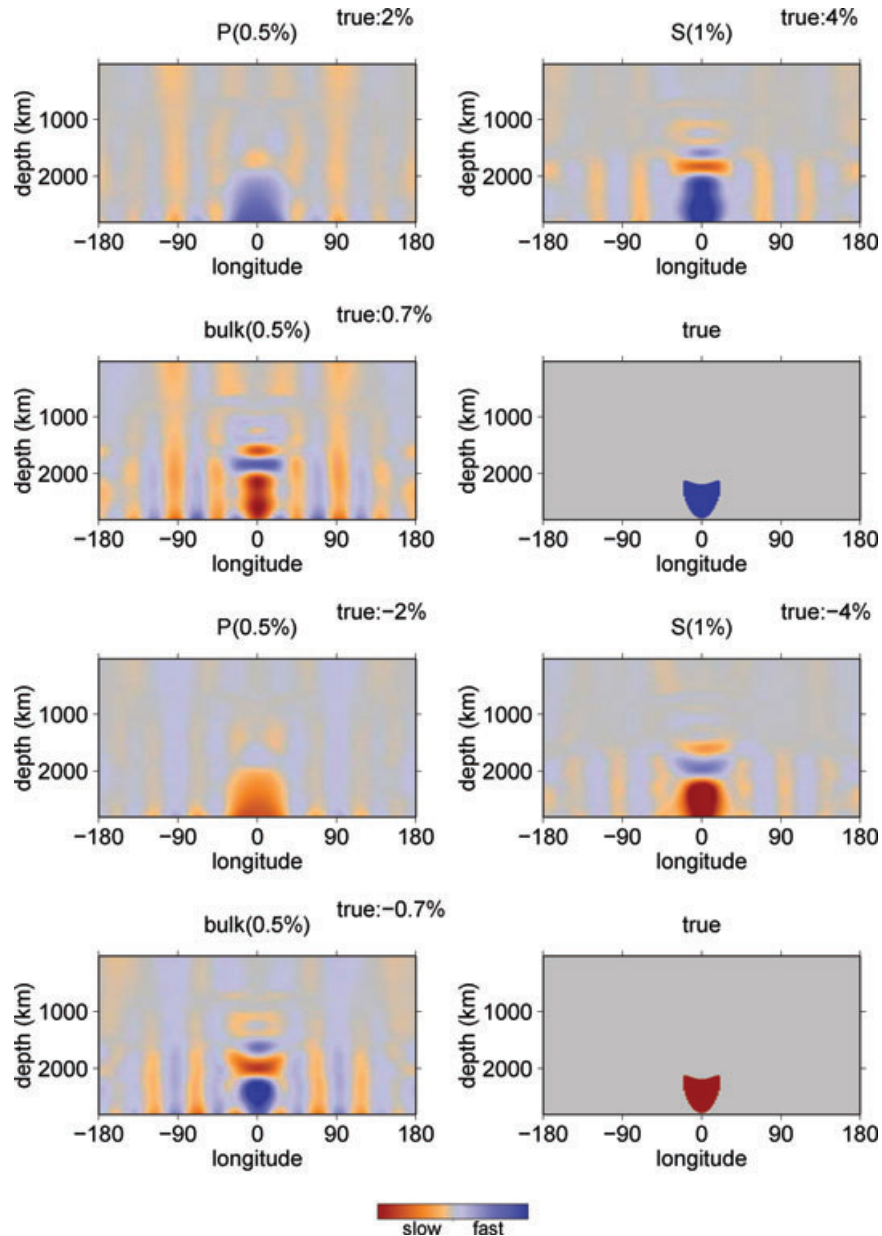


**Figure 19.** Inversion results, at the equator. The number in brackets gives the maximum values of the colour scale for the anomaly; the true number is also given in the title. The ‘true’ plots show the correct anomaly. Note in particular that the bulk anomaly has the incorrect sign for both fast and slow perturbations.

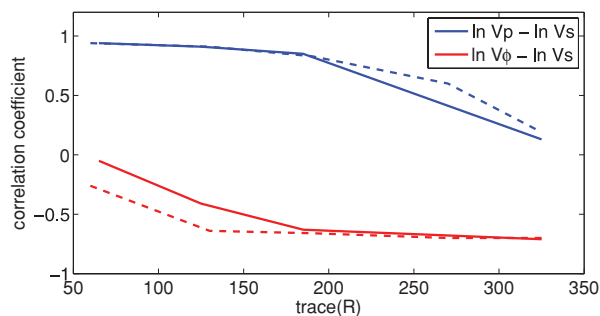


**Figure 20.** Correlation between the recovered velocity anomalies for  $P$  and  $S$  (blue) and for bulk and  $S$  (red) for the slow (solid lines) and fast (dashed lines) anomalies computed 300 km above the CMB at latitude  $0^\circ$  and longitude  $0^\circ$  as a function of resolution [trace ( $R$ )]. The choice of regularization does not seem to effect the sign of the recovered bulk anomaly.

the mathematical physics community. The impact of this effect on both ray- and finite-frequency kernel traveltime inversions is not as simple as previously stated. We find that rather than a systematic bias towards a faster Earth, standard techniques result in a more complicated, though still unphysical, relationship between healed traveltimes and actual perturbations of Earth properties. In particular, from our studies of healing of elastic waves, we conclude that composite properties such as the bulk velocity must be interpreted carefully to avoid bias.

## ACKNOWLEDGMENTS

We are grateful to Fernando Reitich for his help in the development of the boundary integral codes. Most of this work was done while AM was a postdoc at Utrecht University, and was funded

by the Dutch National Science Foundation under grant number NWO:VICI865.03.007.

## REFERENCES

- Babič, V.M. & Buldyrev, V.S., 1972. *Short-Wavelength Diffraction Theory*, Springer Series of Wave Phenomena, Springer-Verlag, Berlin.
- Bolton, H. & Masters, G., 2001. Travel times of P and S from the global digital seismic networks: implications for the relative variation of P and S velocity in the mantle, *J. geophys. Res.*, **106**(B7), 13 527–13 540.
- Bruno, O. & Kunyansky, L., 2001. A fast, high-order algorithm for the solution of surface scattering problems: basic implementation, tests and application, *J. Comput. Phys.*, **169**, 80–110.
- Chapko, R., 2004. On the numerical solution of a boundary value problem in the plane elasticity for a double-connected domain, *Math. Comput. Simulat.*, **66**(4–5), 425–438.
- Chapman, C.H. & Phinney, R.A., 1972. Diffracted seismic signals and their numerical solution, in *Methods in Computational Physics*, Vol. 12, pp. 165–230, Academic Press, New York.
- Claerbout, J.F., 1976. *Fundamentals of Geophysical Data Processing*, McGraw-Hill, New York, NY.
- Claerbout, J.F., 1985. *Imaging the Earth's Interior*, Blackwell Science, Oxford.
- Colton, D. & Kress, R., 1998. *Inverse Acoustic and Electromagnetic Scattering Theory*, Springer-Verlag, Berlin.
- Dziewonski, A.M. & Anderson, D.L., 1981. Preliminary reference earth model, *Phys. Earth planet. Inter.*, **25**(4), 297–356.
- Franz, W., 1954. Über die greenschen funktionen des zylinders und der kugel, *Zeit. Für Naturf.*, **9a**, 705–716.
- Gudmundsson, O., 1996. On the effect of diffraction on traveltime measurements, *Geophys. J. Int.*, **124**, 304–314.
- Hung, S., Dahlen, F. & Nolet, G., 2001. Wavefront healing: a banana-doughnut perspective, *Geophys. J. Int.*, **146**, 289–312.
- Hutko, A.R., Lay, T., Revenaugh, J. & Garnero, E.J., 2008. Anticorrelated seismic velocity anomalies from post-perovskite in the lowermost mantle, *Science*, **320**, 1070–1074.
- Keller, J., 1956. Journal of fluid mechanics digital archive 2006bai, *IRE Trans. Antennas Propagat.*, **4**, 312–321.
- Keller, J., 1962. Geometrical theory of diffraction, *J. Opt. Soc. Am.*, **52**(2), 116.
- Keller, J., 1985. One hundred years of diffraction theory, *IEEE Trans. Antennas Propagat.*, **33**(2), 123–126.
- Klem-Musatov, K., Aizenberg, A., Pajchel, J. & Helle, H.B., 2008. *Edge and Tip Diffractions: Theory and Applications in Seismic Prospecting*, SEG, Tulsa, USA.
- Komatitsch, D. & Tromp, J., 2002a. Spectral-element simulations of global seismic wave propagation—I. Validation, *Geophys. J. Int.*, **149**, 390–412.
- Komatitsch, D. & Tromp, J., 2002b. Spectral-element simulations of global seismic wave propagation—II. 3-D models, oceans, rotation, and gravity, *Geophys. J. Int.*, **150**, 303–318.
- Lomax, A., 1994. The wavelength-smoothing method for approximating broad-band wave propagation through complicated velocity structures, *Geophys. J. Int.*, **117**, 313–334.
- Marquering, H., Nolet, G. & Dahlen, F.A., 1998. Three-dimensional wave-form sensitivity kernels, *Geophys. J. Int.*, **132**, 521–534.
- Marquering, H., Dahlen, F.A. & Nolet, G., 1999. Three-dimensional sensitivity kernels for finite-frequency travel times: the banana doughnut paradox, *Geophys. J. Int.*, **137**, 805–815.
- Martin, P.A., 1990. On the scattering of elastic waves by an elastic inclusion in two dimensions, *Quart. J. Mech. Appl. Math.*, **43**(3), 275–291.
- Masters, G., Laske, G., Bolton, H. & Dziewonski, A., 2000. The relative behavior of shear velocity, bulk sound speed, and compressional velocity in the mantle: Implications for chemical and thermal structure, in *Earth's Deep Interior*, AGU Monographs Vol. 117 eds Karato, S., Forte, A., Liebermann, R., Masters, G. & Stixrude, L., AGU, Washington, DC.
- Montelli, R., Nolet, G., Masters, G., Dahlen, F.A. & Hung, S.-H., 2004. Global P and PP traveltime tomography: rays versus waves, *Geophys. J. Int.*, **158**, 637–654.
- Müller, G., Roth, M. & Korn, M., 1992. Seismic-wave traveltimes in random media, *Geophys. J. Int.*, **110**, 29–41.
- Nolet, G. & Dahlen, F.A., 2000. Wave front healing and the evolution of seismic delay times, *J. geophys. Res.*, **105**(B8), 19 043–19 054.
- Nolet, G. & Moser, T.-J., 1993. Teleseismic delay times in a 3-D earth and a new look at the s-discrepancy, *Geophys. J. Int.*, **114**, 185–195.
- Nussenzveig, H.M., 1992. *Diffraction Effects in Semiclassical Scattering*, Cambridge University Press, Cambridge.
- Ritsema, J., van Heijst, H. & Woodhouse, J., 2004. Global transition zone tomography, *J. geophys. Res.*, **109**, B02302, doi:10.1029/2003JB002610
- Sanchez-Sesma, F. & Campillo, M., 1991. Diffraction of p, sv, and rayleigh waves by topographic features: a boundary integral formulation, *Bull. seism. Soc. Am.*, **81**(6), 2234–2253.
- Snieder, R., 1998. The evolution of phase fronts and the method of strained coordinates, *J. acoust. Soc. Am.*, **103**, 3180–3183.
- Spetzler, J. & Snieder, R., 2001. The effect of small-scale heterogeneity on the arrival time of waves, *Geophys. J. Int.*, **145**, 786–796.
- Thore, P.D. & Juliard, C., 1999. Fresnel zone effect on seismic velocity resolution, *Geophysics*, **64**(2), 593–603.
- Tibuleac, I.M., Nolet, G., Caryl, M. & Koulakov, I., 2003. P wave amplitudes in a 3-D earth, *Geophys. J. Int.*, **155**(1), 1–10.
- To, A. & Romanowicz, B., 2009. Finite frequency effects on global S diffracted traveltimes, *Geophys. J. Int.*, **179**, 1645–1657.
- Tong, J., Dahlen, F.A., Nolet, G. & Marquering, H., 1998. Diffraction effects upon finite-frequency travel times: a simple 2D example, *Geophys. Res. Lett.*, **25**(11), 1983–1986.
- Wielandt, E., 1987. On the validity of the ray approximation for interpreting delay times, in *Seismic Tomography*, pp. 85–98, ed. Nolet, G., D. Reidel Publishing Company, Dordrecht.

## APPENDIX A: NUMERICAL PROCEDURE

As mentioned in the main text, we chose to do the 2-D simulations with a boundary integral method because of its high accuracy for problems involving only a few simple scatterers with small contrasts in material parameters. These appendices provide only a summary, with references to more detailed descriptions of various aspects of the procedures used.

### A1 Acoustic case

The scheme used for the acoustic case is discussed in detail in section 3.5 of Colton & Kress (1998), here we give only a summary and an extension to penetrable obstacles. We begin from the basic equations for the field in both the internal (within the inclusions, denoted  $D$ ) and external (outside the inclusions, denoted  $D^c$ ) domains. The field in each of these domains is split into two parts: the known incident field, which is the field in the absence of a scatterer, and the unknown scattered field, which is the difference between the incident and total fields.

In other words, we seek the solution of

$$\begin{aligned}\Delta\psi_e^s + k_e^2\psi_e^s &= 0 \text{ in } D^c \\ \Delta\psi_i^s + k_i^2\psi_i^s &= 0 \text{ in } D \\ \Delta\psi_e^{\text{inc}} + k_e^2\psi_e^{\text{inc}} &= f \text{ in } D^c \\ \Delta\psi_i^{\text{inc}} + k_i^2\psi_i^{\text{inc}} &= f \text{ in } D\end{aligned}\tag{A1}$$

with boundary conditions that require the continuity of the field and its normal derivative across the interface as well as the standard Sommerfeld radiation condition at infinity. In the above, subscript  $e$  indicates that a quantity is external to the inclusions and subscript  $i$  that it is inside the inclusions, the superscript  $s$  denotes the scattered field and superscript  $\text{inc}$  denotes the incident field. The total field is given by  $\psi = \psi^{\text{inc}} + \psi^s$  for both the internal and external fields and the source function is denoted by  $f$ .

As the name suggests, in integral methods we solve an integral equation, rather than the differential equations given in (A1). To that end, we use Green's theorem to write

$$\psi_i^s(x) = \int_{\partial D} G_i(x-y) \frac{\partial \psi_i^s}{\partial n_y}(y) - \frac{\partial G_i}{\partial n_y}(x-y) \psi_i^s(y) dy \quad x \in D \tag{A2}$$

$$0 = \int_{\partial D} G_i(x-y) \frac{\partial \psi_i^{\text{inc}}}{\partial n_y}(y) - \frac{\partial G_i}{\partial n_y}(x-y) \psi_i^{\text{inc}}(y) dy \quad x \in D \tag{A3}$$

for the interior field, where  $G_i$  is the Green's function for the interior domain,  $D$ , defined by

$$\Delta G_i^{\text{inc}} + k_i^2 G_i^{\text{inc}} = -\delta \text{ in } D \tag{A4}$$

with  $G_e$  defined similarly in the exterior domain,  $D^c$ . We denote by  $\frac{\partial}{\partial n_y}$  the normal derivative with respect to  $y$  with outward normal and by  $\partial D$  the boundary of  $D$ . The analogous expressions for the exterior field are

$$\psi_e^s(x) = \int_{\partial D} \frac{\partial G_e}{\partial n_y}(x, y) \psi_e^s(y) - G_e(x, y) \frac{\partial \psi_e^s}{\partial n_y}(y) dy \quad x \in D^c \tag{A5}$$

$$0 = \int_{\partial D} \frac{\partial G_e}{\partial n_y}(x-y) \psi_e^{\text{inc}}(y) - G_e(x-y) \frac{\partial \psi_e^{\text{inc}}}{\partial n_y}(y) dy \quad x \in D^c. \tag{A6}$$

To derive an integral equation valid on the *surface* of the inclusions, we take the limit as  $x \rightarrow \partial D$  which gives

$$1/2 \psi_i^s(x) = \int_{\partial D} G_i(x, y) \frac{\partial \psi_i^s}{\partial n_y}(y) - \frac{\partial G_i}{\partial n_y}(x, y) \psi_i^s(y) dy \quad x \in \partial D \tag{A7}$$

$$-1/2 \psi_i^{\text{inc}}(x) = \int_{\partial D} G_i(x, y) \frac{\partial \psi_i^{\text{inc}}}{\partial n_y}(y) - \frac{\partial G_i}{\partial n_y}(x, y) \psi_i^{\text{inc}}(y) dy \quad x \in \partial D \tag{A8}$$

for the interior field and

$$1/2 \psi_e^s(x) = \int_{\partial D} \frac{\partial G_e}{\partial n_y}(x, y) \psi_e^s(y) - G_e(x, y) \frac{\partial \psi_e^s}{\partial n_y}(y) dy \quad x \in \partial D \tag{A9}$$

$$-1/2 \psi_e^{\text{inc}}(x) = \int_{\partial D} \frac{\partial G_e}{\partial n_y}(x, y) \psi_e^{\text{inc}}(y) - G_e(x, y) \frac{\partial \psi_e^{\text{inc}}}{\partial n_y}(y) dy \quad x \in \partial D \tag{A10}$$

for the external field.

We now add (A7)–(A10) and apply the boundary conditions to the result giving

$$\psi_e(x) = \psi^{\text{inc}}(x) + \int_{\partial D} \frac{\partial(G_i - G_e)}{\partial n_y}(x, y) \psi_e(y) - (G_i - G_e)(x, y) \frac{\partial \psi_e}{\partial n_y}(y) dy, \tag{A11}$$

recalling that  $\psi_e = \psi_e^{\text{inc}} + \psi_e^s$  and defining  $\psi^{\text{inc}} = \psi_i^{\text{inc}} + \psi_e^{\text{inc}}$ . A similar procedure applied to the normal derivatives of the initial equations leads to

$$\frac{\partial \psi_e}{\partial n_x}(x) = \frac{\partial \psi^{\text{inc}}}{\partial n_x}(x) + \int_{\partial D} \frac{\partial^2(G_i - G_e)}{\partial n_x \partial n_y}(x, y) \psi_e(y) - \frac{\partial_x(G_i - G_e)}{\partial n_x}(x, y) \frac{\partial \psi_e}{\partial n_y}(y) dy. \tag{A12}$$

The coupled system of (surface) integral equations (A11) and (A12) provides a complete mathematical formulation of the propagation of a single frequency for an arbitrary source function,  $f$ . Once these are resolved, the field at any point in space can be recovered from eqs (A2)–(A8).

The numerical solution of this system, on the other hand, is complicated by the singular nature of the Green's functions (which demand a careful design of quadrature formulas for accurate evaluation) and their long range effects (which translate into 'full' matrices upon discretization, necessitating the use of acceleration techniques for efficiency). To overcome the former difficulty we resort to spectral



quadratures as defined in Colton & Kress (1998, pp. 67–78) for the 2-D case. To briefly summarize this method, we first separate the singular part of the integral, dividing  $G$  into  $G_1$  and  $G_2$  where

$$G(t, \tau) = G_1(t, \tau) \ln \left[ 4 \sin^2 \left( \frac{t - \tau}{2} \right) \right] + G_2(t, \tau), \quad (\text{A13})$$

where both  $G_1$  and  $G_2$  are analytic and  $t$  is the parametrization of the anomaly in  $x$  and  $\tau$  in  $y$ . The integration of  $G_2$  is then straightforward as it is a smooth periodic function the trapezoidal rule is spectrally accurate. To integrate  $G_1(t, \tau) \ln \left( 4 \sin^2 \frac{t - \tau}{2} \right)$  we make use of the rule

$$\int_0^{2\pi} G_1(t, \tau) \ln \left[ 4 \sin^2 \left( \frac{t - \tau}{2} \right) \right] d\tau \approx \sum_{j=0}^{2n-1} R_j^{(n)}(t) G_2(t, t_j), \quad (\text{A14})$$

where

$$R_j^{(n)}(t) := -\frac{2\pi}{n} \sum_{m=1}^{n-1} \frac{1}{m} \cos[m(t - t_j)] - \frac{\pi}{n^2} \cos[n(t - t_j)]. \quad (\text{A15})$$

Note that in determining  $G_1$  and  $G_2$  the values at  $t = \tau$  must be determined separately by explicitly taking the limits. In Bruno & Kunyansky (2001) these ideas are extended to the 3-D case.

## A2 Elastic case

The extension of the results discussed in the previous section to the elastic case requires two key components. The first is an expression for the Green's function in an elastic media and the second is an understanding of the singularities in this Green's function and how to accurately and efficiently compute the resulting integrals.

In Sanchez-Sesma & Campillo (1991) the Green's function is given [their eqs (8) and (9)]; they also give explicitly its singular structure. For completeness and to introduce some notation we repeat the Green's function,  $G$  and tractions  $T$

$$\begin{aligned} G_{22} &= \frac{1}{i4\rho} \frac{H_0(k_s r)}{\beta^2}, \\ G_{mn} &= \frac{1}{i8\rho} [\delta_{mn} A - (2\gamma_m \gamma_n - \delta_{mn}) B], \\ T_{22} &= \frac{i}{4r} D(k_s r) \gamma_k n_k \\ T_{mn} &= \frac{i\mu}{2\rho r} \left\{ \left[ B + \frac{\lambda D(k_p r)}{2\mu\alpha^2} \right] \gamma_n n_m + \left[ B + \frac{D(k_s r)}{2\beta^2} \right] (\gamma_n n_m + \gamma_k n_k \delta_{mn}) \right. \\ &\quad \left. + (C - 4B) \gamma_m \gamma_n \gamma_k n_k \right\}, \end{aligned} \quad (\text{A16})$$

where

$$\begin{aligned} A &= \frac{H_0(k_p r)}{\alpha^2} + \frac{H_0(k_s r)}{\beta^2} \\ B &= \frac{H_2(k_p r)}{\alpha^2} - \frac{H_2(k_s r)}{\beta^2} \\ C &= \frac{D(k_p r)}{\alpha^2} - \frac{D(k_s r)}{\beta^2} \end{aligned} \quad (\text{A17})$$

$$D(p) = p H_1(p)$$

and  $\rho$  is the density,  $\lambda$  and  $\mu$  are Lamé's parameters,  $\alpha = \sqrt{(\lambda + 2\mu)/\rho}$  is the  $P$ -wave velocity,  $\beta = \sqrt{\mu/\rho}$  is the  $S$ -wave velocity,  $k_s = \omega/\beta$  is the  $S$  wavenumber and  $k_p = \omega/\alpha$  is the  $P$  velocity. The Hankel function of order  $q$  is denoted by  $H_q$ ; whether Hankel functions of the first or second kind are used depends on Fourier sign conventions, we choose the first kind. We use the Einstein summation convention so that  $\gamma_k n_k = \vec{\gamma} \cdot \vec{n}$ ; the indices  $m, n$  are 1 and 3 with 2 being dealt with separately. The vector  $\vec{n}$  is the unit outward normal to the surface,  $r = \sqrt{(x_1 - y_1)^2 + (x_3 - y_3)^2}$  is the distance function where  $y$  will be the integration variable and  $x$  the output point;  $\gamma_m = (x_m - y_m)/r$  and  $\delta_{mn}$  is the kronecker delta.

As stated in Sanchez-Sesma & Campillo (1991), the form in eqs (A16) and (A17) highlights immediately the singular structure of the Green's function and Tractions. The Green's function itself has a logarithmic singularity as is seen from the asymptotic expansion of the Hankel function (see, among many others, Colton & Kress 1998, p. 64). Similarly, in this form, the tractions have  $1/r$  singularities. As in the acoustic case, when we needed to compute  $\frac{\partial^2(G_i - G_e)}{\partial n_x \partial n_y}$  for the elastic case we will require the traction applied to the traction. Following

Martin (1990) this is given by

$$\begin{aligned}
 N_{mn} := & \frac{4}{\mu i} [T^x T^y G(x, y)]_{mn} = k_s^2 g^2 n_m(y) n_n(x) H_0(k_s r) \\
 & + \frac{2}{r} (\mathcal{N} \delta_{mn} + n_m(x) n_n(y)) H_1(k_s r) + \frac{4g}{r} n_m(y) n_n(x) H_1(k_p r) \\
 & - [\mathcal{N} X_{mn} + \Theta \delta_{mn} + B_{mn}(x, y) + B_{nm}(y, x)] H_2(k_s r) - 2g [B_{nm}(x, y) + B_{mn}(y, x)] H_2(k_p r) \\
 & - 4k_s^{-2} \{ r^{-2} [\mathcal{N} \delta_{mn} + n_m(x) n_n(y) + n_m(y) n_n(x)] F_2 - r^{-1} [\mathcal{N} X_{mn} + \Theta \delta_{mn} \\
 & + B_{mn}(x, y) + B_{nm}(x, y) + B_{mn}(y, x) + B_{nm}(y, x)] F_3 + \Theta X_{mn} F_4 \}, \quad (A18)
 \end{aligned}$$

where  $g = \nu/(1 - \nu) = \lambda/(\lambda + 2\mu)$ ,  $\mathcal{N} = n(x) \cdot n(y)$ ,  $X_{mn} = \gamma_m \gamma_n$ ,  $\Theta = n_j(x) n_k(y) \gamma_j \gamma_k$ ,  $B_{mn}(x, y) = n_m(x) n_j(y) \gamma_j \gamma_n$ ,  $F_j = k_s^j H_j(k_s r) - k_p^j H_j(k_p r)$  and the superscript on  $T$  indicates the variable in which it is applied. In eq. (A18) the most singular terms have singularities of  $r^{-2}$ ; this is shown in Martin (1990) where the singular structure is also given explicitly as

$$-2r^{-2} (g_2 \mathcal{N} \delta_{mn} + (1 - g_2) \mathcal{N} X_{mn} + A n_m(x) n_n(y) + [1 - 3A] n_m(y) n_n(x)), \quad (A19)$$

where  $g_2 = \frac{1-2\nu}{2(1-\nu)}$ . Martin then shows that for the two-medium problem studied here

$$\hat{N} := (1 - \nu^i) N^i - (1 - \nu^e) N^e \quad (A20)$$

has only a  $r^{-1}$  singularity, where we use superscripts for the interior and exterior fields to distinguish these from the matrix subscripts. Eq. (A20) takes the place of  $G_e - G_i$  in the previous section. In that case we were able to reduce the singularity to logarithmic whereas here it is only possible to obtain an  $r^{-1}$  singularity.

We now give the necessary equations to solve for the elastic field due to an inclusion with  $C^2$  boundary. For the displacement, analogous to eq. (A11) we have

$$u_m(x) = u_m^{\text{inc}}(x) + \int_{\partial D} (G_{mn}^e - G_{mn}^i)(x, y) t_n(y) - (T_{mn}^{e,y} - T_{mn}^{i,y})(x, y) u_n(y) dy \quad x \in \partial D, \quad (A21)$$

and for the tractions we have

$$\begin{aligned}
 t_m(x) = & (1 - \nu^i) t_m^{\text{inc}}(x) - (1 - \nu^e) t_m^{\text{inc}}(x) \\
 & + \int_{\partial D} \left( \frac{1 - \nu^i}{\mu^i} T_{mn}^{i,x} - \frac{1 - \nu^e}{\mu^e} T_{mn}^{e,x} \right) (x, y) t_n(y) - \hat{N}_{mn} u_n(y) dy \quad x \in \partial D. \quad (A22)
 \end{aligned}$$

To solve this system we set-up the following matrix equation

$$\begin{bmatrix} u_1 \\ u_3 \\ t_1 \\ t_3 \end{bmatrix} = \begin{bmatrix} u_1^{\text{inc}} \\ u_3^{\text{inc}} \\ t_1^{\text{inc}} \\ t_3^{\text{inc}} \end{bmatrix} + \begin{bmatrix} G_{11}^e - G_{11}^i & G_{13}^e - G_{13}^i & T_{11}^{e,y} - T_{11}^{i,y} & T_{13}^{e,y} - T_{13}^{i,y} \\ G_{31}^e - G_{31}^i & G_{33}^e - G_{33}^i & T_{31}^{e,y} - T_{31}^{i,y} & T_{33}^{e,y} - T_{33}^{i,y} \\ \frac{1-\nu^e}{\mu^e} T_{11}^{e,x} - \frac{1-\nu^i}{\mu^i} T_{11}^{i,x} & \frac{1-\nu^e}{\mu^e} T_{13}^{e,x} - \frac{1-\nu^i}{\mu^i} T_{13}^{i,x} & \hat{N}_{11} & \hat{N}_{13} \\ \frac{1-\nu^e}{\mu^e} T_{31}^{e,x} - \frac{1-\nu^i}{\mu^i} T_{31}^{i,x} & \frac{1-\nu^e}{\mu^e} T_{33}^{e,x} - \frac{1-\nu^i}{\mu^i} T_{33}^{i,x} & \hat{N}_{31} & \hat{N}_{33} \end{bmatrix} \begin{bmatrix} u_1 \\ u_3 \\ t_1 \\ t_3 \end{bmatrix} \quad (A23)$$

and solve it directly using its LU factorization. From this solution using that

$$u_m^e(x) = u_m^{\text{inc}}(x) + \int_{\partial D} G_{mn}^e(x, y) t_n^e(y) - T_{mn}^e(x, y) u_n^e(y) dy \quad x \in D^c \quad (A24)$$

and

$$u_m^i(x) = u_m^{\text{inc}}(x) - \int_{\partial D} G_{mn}^i(x, y) t_n^i(y) - T_{mn}^i(x, y) u_n^i(y) dy \quad x \in D \quad (A25)$$

we obtain the field at any point within the domain.

The fact that both the traction and  $\hat{N}$  have  $r^{-1}$  singularities requires different discretization weights than those used in the acoustic case. Rather than separating each operator into a smooth and logarithmically singular part, we now separate each operator into three parts

$$T(t, \tau) = T_1(t, \tau) \ln \left[ 4 \sin^2 \left( \frac{t - \tau}{2} \right) \right] + T_2(t, \tau) + T_3(t, \tau) \cot \left( \frac{t - \tau}{2} \right), \quad (A26)$$

where  $T_1$  and  $T_2$  are dealt with in the same manner as  $G_1$  and  $G_2$  were for the acoustic case. For  $T_3$ , following Chapko (2004), we separate

out the  $r^{-1}$  singularity and then compute

$$\begin{aligned} \int_0^{2\pi} T_3(t, \tau) \cot\left(\frac{t-\tau}{2}\right) d\tau &= \int_0^{2\pi} T_{3a}(t, \tau) \tan\left(\frac{t-\tau}{2}\right) \cot\left(\frac{t-\tau}{2}\right) d\tau \\ &\approx \sum_{j=0}^{2*n-1} T_j^{(n)}(t) T_3\left[t, t_j^{(n)}\right], \end{aligned} \quad (\text{A27})$$

where

$$T_j^{(n)} = \frac{1}{n} \sum_{m=1}^{n-1} \sin\left[m\left(t - t_j^{(n)}\right)\right] - \frac{1}{2n} \sin\left[n\left(t - t_j^{(n)}\right)\right]. \quad (\text{A28})$$

In this formulation, we take advantage of the fact that  $\tan[(t - \tau)/2]/r$  is regular at  $t = \tau$  so that  $T_3(t, \tau)$  is regular at this point. The singularity is then moved into the cot term where it can be dealt with using the quadrature given in eq. (A28).